

Self-field quench behavior of multifilamentary MgB₂ wires in liquid helium

X. Wang^{a,b,c,1}, S.V.P.S.S. Pamidi^{b,c}, U.P. Trociewitz^c, J. Schwartz^{a,b,c,d,*}

^a Department of Electrical and Computer Engineering, FAMU-FSU College of Engineering, Tallahassee, FL 32310, USA

^b Center for Advanced Power Systems, Florida State University, Tallahassee, FL 32310, USA

^c Applied Superconductivity Center, National High Magnetic Field Laboratory, Tallahassee, FL 32310, USA

^d Department of Mechanical Engineering, FAMU-FSU College of Engineering, Tallahassee, FL 32310, USA

ARTICLE INFO

Article history:

Received 15 January 2008

Received in revised form 19 June 2008

Accepted 24 June 2008

Available online xxx

Keywords:

MgB₂ wires (A)

Quench (C)

Stability (C)

Propagation velocity (C)

ABSTRACT

Self-field quench behavior of two types of multifilamentary MgB₂ wires with different numbers of filaments and outer sheath materials are tested. One sample type has a Glidcop outer sheath and the other has a Monel outer sheath. Samples are bath cooled in liquid helium at 4.2 K. A normal zone is initiated by a heater wound around the sample. Voltage and temperature along the samples are monitored and results from two sample types are compared. For the same transport current and end-to-end voltage, the normal zone length is shorter in the Monel-sheathed sample than that in the Glidcop-sheathed sample, which leads to higher electrical field and temperature gradient in the Monel-sheathed sample. The relationship between the voltage and hot-spot temperature is discussed for both samples. Quench energy and normal zone propagation velocity are measured at different transport currents and compared with the existing data for similar samples measured in an adiabatic environment.

© 2008 Elsevier Ltd. All rights reserved.

1. Introduction

MgB₂ is an emerging conductor of technical interest because it can be readily made as an untextured wire without weak links and with the potential for low cost [1–5]. Significant progress in conductor development and prototype demonstration has been made in MgB₂ since its discovery and a number of industrial manufacturers are emerging [6–20].

For successful large scale applications, quench behavior of the conductor must be understood. Several quench experiments are reported on MgB₂ wire/tape of different architectures [21–26]. In most cases, samples are cooled adiabatically; few are cooled in liquid helium. A normal zone is initiated by a heater attached to the sample. In these studies, the normal zone propagation velocities are in the range of 0.01–1 m/s and the minimum quench energies are found to be on the order of 10–100 mJ. A normal zone is also initiated by an overcurrent in cryocooled samples to simulate the fault current in a power system [27]. The experimental results are compared to several computational models and good agreement is found [23–26]. The quench behavior of both multifilamentary MgB₂ tapes with a ferromagnetic matrix and coils wound by

similar conductors were investigated computationally [28,29]. The effect of the materials and thickness of the stabilizer on the stability of MgB₂ wires were simulated [30,31].

In this paper, we report the self-field quench behavior of two multifilamentary MgB₂ round wires in liquid helium at 4.2 K. The goal is to investigate the quench behavior of the evolving MgB₂ conductors and its impact on the quench detection and protection system for application based on this conductor. The experimental approach is presented first. Typical voltage and temperature profiles of a quench and recovery are shown. Given the same transport current and the voltage across the sample, the normal zone length is estimated for both samples. Its implication for quench detection and protection is discussed. Also discussed is the relationship between the voltage and temperature during the quench for both samples. In the end, the results of minimum quench energy and normal zone propagation velocity are presented and compared to the existing data, and in particular to data on similar samples measured in-field and in an adiabatic environment.

2. Experimental approach

2.1. MgB₂ wires

Two types of multifilamentary MgB₂ wire samples (∅0.83 mm) are provided by Hyper Tech Research Inc. The samples were received in July 2006 and are typical of samples of that time frame. The first sample is oxide-dispersion strengthened Cu (Glidcop)-sheathed (CS) and has six MgB₂ filaments. The second sample is

* Corresponding author. Address: Department of Electrical and Computer Engineering, FAMU-FSU College of Engineering, Tallahassee, FL 32310, USA.

E-mail addresses: xrwang@lbl.gov (X. Wang), pamidi@caps.fsu.edu (S.V.P.S.S. Pamidi), trociew@magnet.fsu.edu (U.P. Trociewitz), schwartz@magnet.fsu.edu (J. Schwartz).

¹ Present address: Lawrence Berkeley National Laboratory, 1 Cyclotron Road, Mail Stop 46-161, Berkeley, CA 94720, USA.

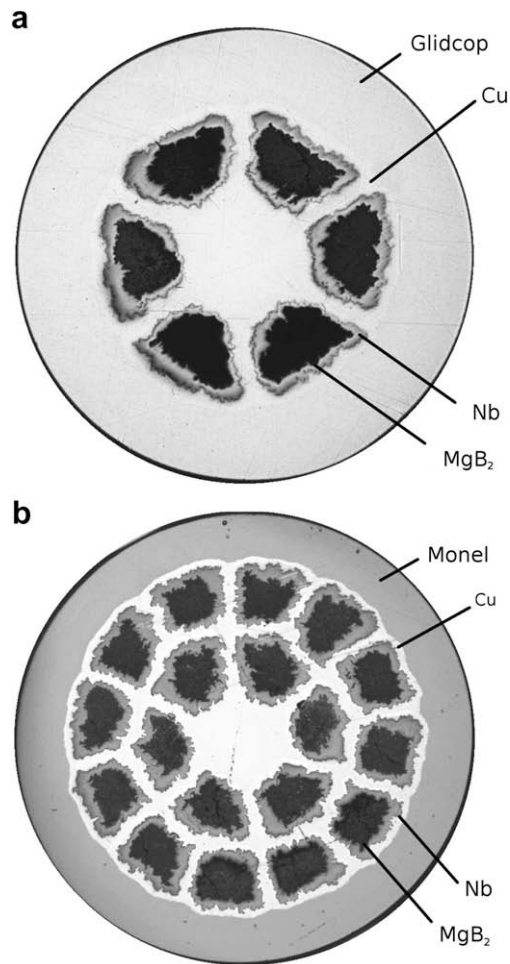


Fig. 1. Optical micrographs of the cross-section of (a) a Glidcop-sheathed sample with six filaments and (b) a Monel-sheathed sample with 18 filaments. Both samples have a Cu matrix.

Table 1
Sample parameters

Name	Filaments	Outer sheath	Fill factor	I_c (4.2 K, s.f.) (A)	Nominal filament area (mm ²)
CS	6	Glidcop	0.16	900	0.014
MS	18	Monel	0.17	1000	0.005

CuNi (Monel)-sheathed (MS) and has 18 filaments. Both samples have a Cu matrix. Fig. 1 shows the wire cross-sections and Table 1 lists their parameters. More details of the wire can be found in [6,7]. The critical currents in Table 1 are measured by Hyper Tech Research Inc. using an ITER barrel on samples that are in the same batch of the samples tested in this study.

2.2. Measurement setup

Straight wires are cut 14 cm in length and mounted onto a quench probe with a sample holder as shown in Fig. 2a. A 1 cm length at each end of the sample is soldered to the Cu current leads. Another 1 cm is left between the end of the current contact and the nearest voltage tap to minimize the effects of current transfer [32–34]. Six voltage taps are soldered to the sample surface with a 2 cm spacing. Thermocouples are attached between the voltage taps. Fig. 2 shows an instrumented sample and the configuration of the voltage taps and thermocouples.

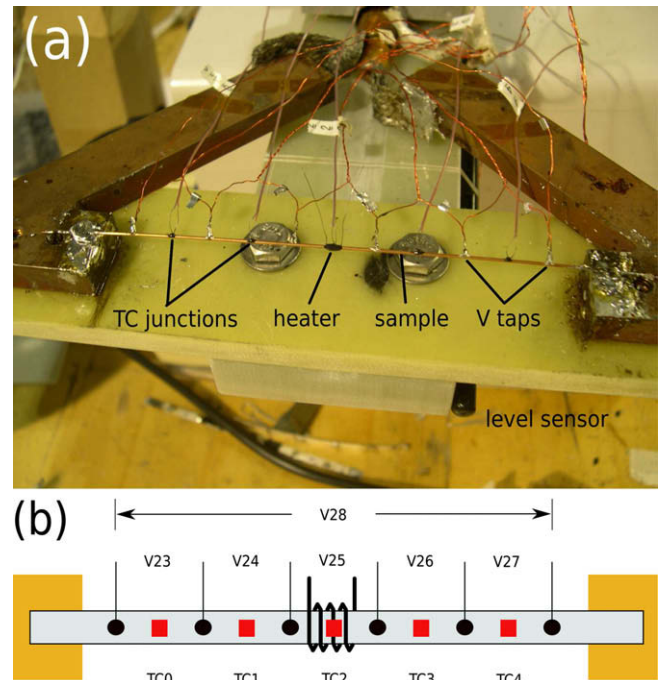


Fig. 2. (a) An instrumented sample mounted on the quench probe. (b) Schematic of voltage taps and thermocouples along the sample.

NiCr wire ($\varnothing 0.16$ mm) with a single polyimide insulation layer is wound around the middle section of the wire for 12 tight turns to make the heater (see Fig. 3). The heater is about 3.3 mm long along the sample. The physical dimension of the heater is controlled to be as similar as possible for each sample. Epoxy (Stycast 2850FT) is used to attach the heater around the sample. The epoxy mass is recorded by measuring the difference of the mass before and after attaching the heater.

Type E thermocouples are used to measure the temperature evolution during the experiment. The thermocouple junctions are attached to the middle of each voltage section with epoxy; 0.4–0.9 mg is used to attach each thermocouple junction to the sample.

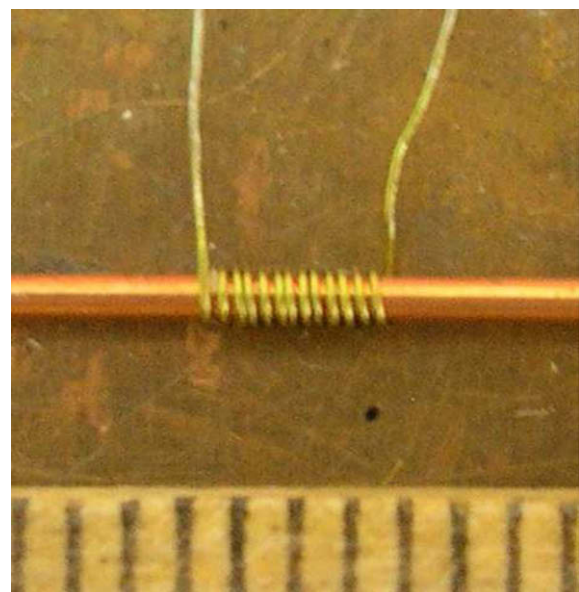


Fig. 3. Insulated NiCr wire wound around the sample to make the heater. The marker interval is 1 mm.

Because the sample is covered by the heater, the thermocouple in section V_{25} is attached to the heater while all the other thermocouples directly contact the sample. The thermocouple junctions are made by welding a pair of thermocouple wires ($\varnothing 0.127$ mm). Cu extension wires ($\varnothing 0.127$ mm) are welded to the thermocouple wires to make the reference junctions which are submerged in liquid nitrogen during the experiment. To determine the thermocouple error, a thermocouple junction was attached to the bottom surface of a calibrated Cernox sensor so that they are close enough to measure the same temperature. The thermocouple error is around -8 K at 4.2 K and within 5 K for higher temperatures up to room temperature.

A 53.3 cm long liquid helium level sensor is fixed along the sample holder, the end of which is seen in Fig. 2a. The helium level is monitored every minute and is maintained at least 12 cm above the sample. Thus the sample is always submerged in liquid helium during the experiment.

The transport current is measured across a precision shunt rated at 1 kA/100 mV. Both $V(t)$ and $T(t)$ along the sample are monitored during the experiment. Voltages across different sections are measured by an array of digital multimeters (DMMs) and a digital phosphor oscilloscope (DPO). The temporal resolution is about 15 ms per data point for each buffered DMM. The resolution for each channel of the oscilloscope is 400 μ s per data point for the MS sample and 10 ms per data point for the CS sample. The DPO monitors the heater voltage, V_{25} , V_{26} , and V_{27} . The voltage signals monitored by the DPO are isolated from each other by an isolation amplifier with the gain set to 1. The thermocouple voltages are scanned by three switch/DMMs with a scanning speed of ~ 16 ms per data point per channel. All the instruments are controlled by a PC running LabView via an IEEE-488 bus. A bus-trigger signal is used to synchronize the instruments.

The experiment is protected by the over-voltage protection capability embedded in the power supply (HP 6681 A). Once the end-to-end voltage (V_{28}) of the sample exceeds a preset value, the power supply shuts off and the transport current drops to zero.

2.3. Test protocol

The experiment begins by establishing a steady-state transport current below the sample I_c given in Table 1. A normal zone is then initiated by pulsing a voltage across the NiCr heater. The pulse voltage has a square waveform with the duration fixed at 300 ms; the amplitude is adjusted to vary to the heat input. Initially, a small pulse voltage amplitude is used. If the sample does not quench, the amplitude is increased until a quench is initiated by the minimum pulse voltage. This is repeated for various transport currents. After the minimum quench voltages are found for different transport currents, the normal zone propagation velocity at each transport current level is measured.

If the sample is degraded by a quench then the pulse voltage required to initiate a quench will decrease. Thus, after each quench, the sample is retested with a fixed transport current and the maximum pulse voltage from which the sample recovered previously. If the sample still recovers, then it is assumed that the sample is not degraded.

3. Results and discussion

3.1. $V(t)$ and $T(t)$ profiles

Fig. 4 shows $V(t)$ and $T(t)$ for the CS sample during a quench with the transport current $I_t = 300$ A ($\sim 33.3\%I_c$). Voltages are increasing across every section along the sample until the power supply is off.

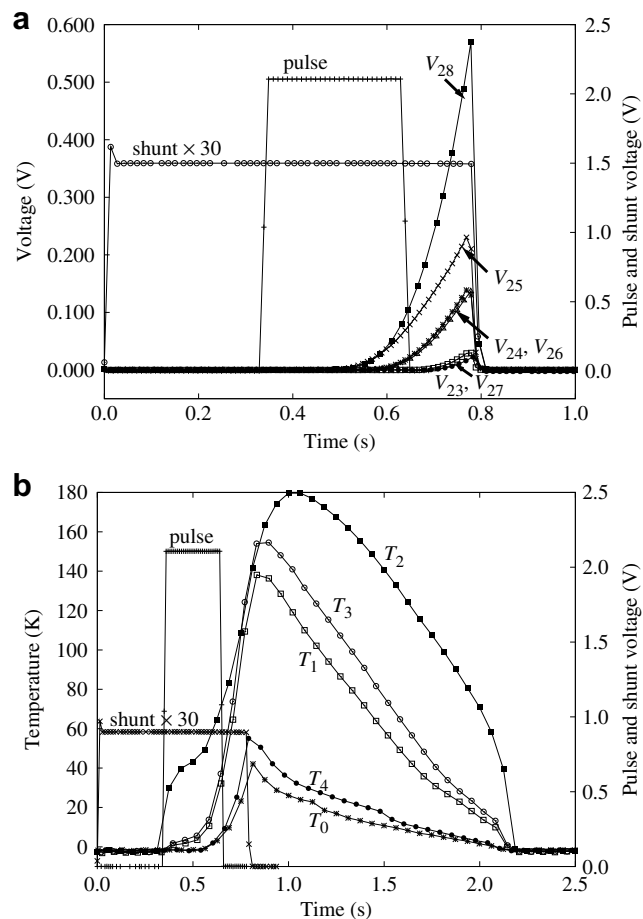


Fig. 4. (a) $V(t)$ and (b) $T(t)$ for a quench in the CS sample with $I_t = 300$ A ($\sim 33.3\%I_c$), 4.2 K, self field. The DPO resolution is 10 ms/pt.

Voltage taps are distributed symmetrically around the heater. This symmetry is seen in almost identical voltages measured at voltage taps of corresponding symmetry. For example, $V_{24}(t)$ and $V_{26}(t)$ overlap. This indicates that the normal zone, after being initiated in the middle section, propagates at the same speed to both ends of the sample, which may also indicate that the sample I_c is uniform along the length. Correspondingly, $T_1(t)$ is close to $T_3(t)$ and $T_0(t)$ pairs $T_4(t)$, as seen in Fig. 4b. Note that T_2 peaks after the power is off with a lag of ~ 270 ms while T_0 and T_4 decrease without significant delay. The further the distance from the heater, the sooner the temperature decreases when the current is off.

Fig. 5 shows the $V(t)$ and $T(t)$ for a recovery measured with $I_t = 150$ A ($\sim 16.7\%I_c$) in the CS sample. The normal zone is initiated and voltages rise across the middle three sections, as shown in Fig. 5a. The normal zone collapses rather than propagating; thus there is no measurable voltage across sections V_{23} and V_{27} . The peak value of V_{28} reaches ~ 24 mV. Unlike the quench case shown in Fig. 4, the $V(t)$ and $T(t)$ in this case have an almost identical time span during which they rise and fall.

3.2. Normal zone length

$V(t)$ and $T(t)$ profiles for both sample types during a quench are compared in Fig. 6. In this case, I_t is 150 A, which corresponds to $\sim 16.7\%I_c$ for the CS sample and $\sim 15.0\%I_c$ for the MS sample. The maximum end-to-end voltage (V_{28}) is set to 0.5 V. The quenches are initiated by the minimum pulse voltage amplitudes for each sample (4.00 V for the CS sample and 3.07 V for the MS

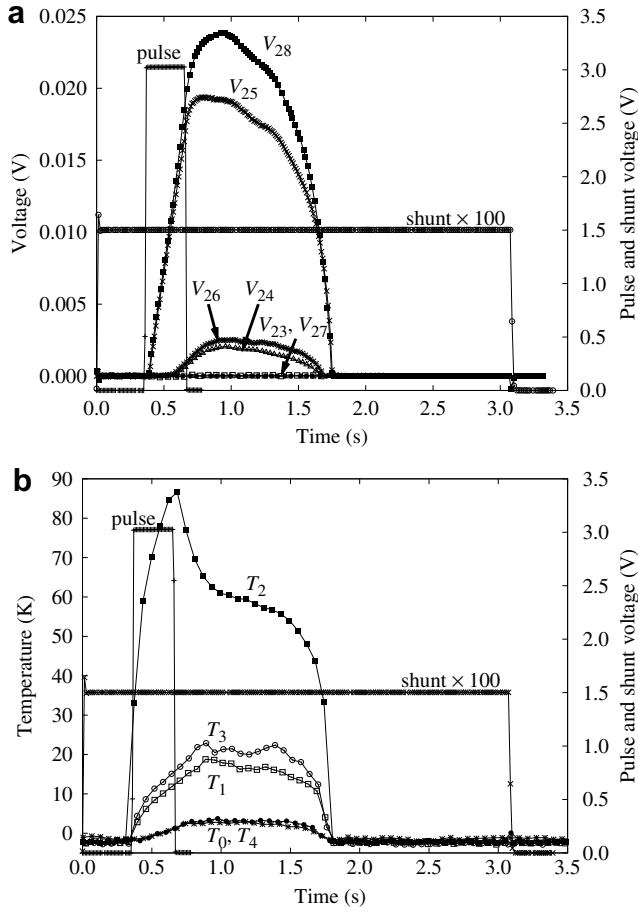


Fig. 5. (a) $V(t)$ and (b) $T(t)$ for a recovery in the CS sample with $I_t = 150$ A ($\sim 16.7\%I_c$), 4.2 K, self field. The DPO resolution is 10 ms/pt.

sample). In Fig. 6, the $V(t)$ and $T(t)$ curves of the MS sample are shifted in time so that the rising edge of the MS pulse overlaps that of the CS pulse.

As shown in Fig. 6a, when the power supply is shut off, there is no voltage across the end section (V_{27}) of the MS sample, while $V_{27} \sim 50$ mV in the CS sample. This indicates that when the end-to-end voltage of both samples reach the same value with the same transport current, the length of the normal zone in the MS sample is shorter than that in the CS sample. The temporal temperature profiles shown in Fig. 6b are consistent with the above discussion.

The spatial temperature profile along the samples, $T(x)$, when the power supply is shut off, are shown in Fig. 7. Assuming that $I_c(T)$ is linear and $T_c = 39$ K, then a transport current of 150 A corresponds to a current sharing temperature (T_{cs}) of 33.2 K for the CS sample and 33.8 K for the MS sample [35]. $T_{cs} = 33.5$ K is used for both samples in the following.

Considering the $T(x)$ profile in Fig. 7, the normal zone length in the CS sample, L_{CS} , is at least 80 mm as the temperature between thermocouples TC0 and TC4 is higher than 33.5 K. In the MS sample, $T_0 = 14$ K and $T_4 = 8$ K, both lower than 33.5 K, even considering the uncertainty of the temperature measurement. So the end sections in the MS sample (V_{23} and V_{27}) are not normal when the power supply is off. By linearly interpolating $T(x)$ between the temperatures at TC0 and TC4, and using $T_{cs} = 33.5$ K, from Fig. 7 one derives $L_{MS} \sim 61$ mm.

Since for both samples $V_{28} \approx 0.5$ V and $I_t = 150$ A, the total end-to-end resistances are equal, i.e.,

$$R_{MS} = R_{CS} = \frac{V_{28}}{I_t}. \quad (1)$$

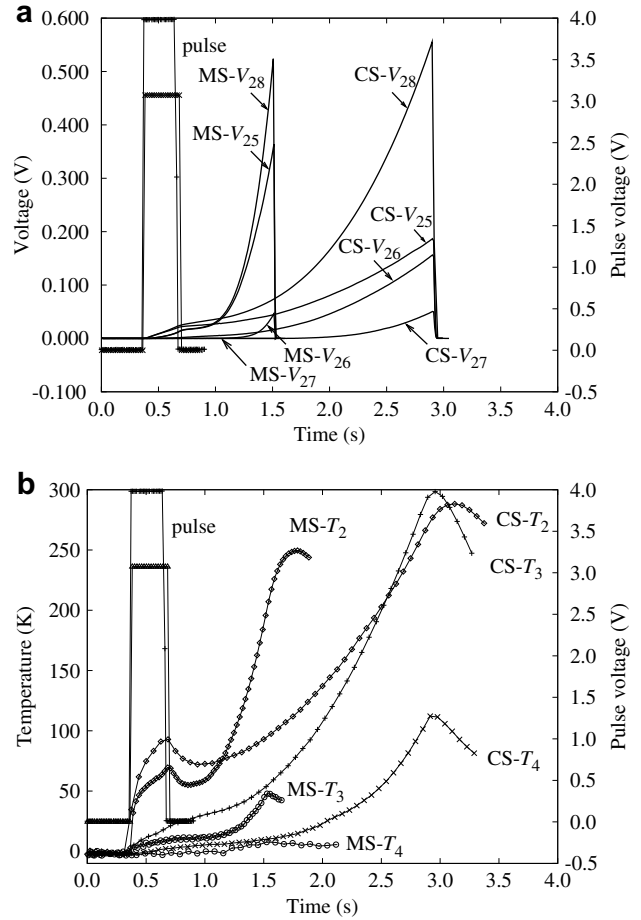


Fig. 6. $V(t)$ and $T(t)$ for each sample type with $I_t = 150$ A, measured in liquid helium at 4.2 K and self-field. (a) $V(t)$ profiles for sections V_{28} , V_{25} , V_{26} , and V_{27} (see Fig. 2b). (b) $T(t)$ profiles corresponding to the $V(t)$ shown in (a). Heater pulse voltages are shown in the secondary y-axis.

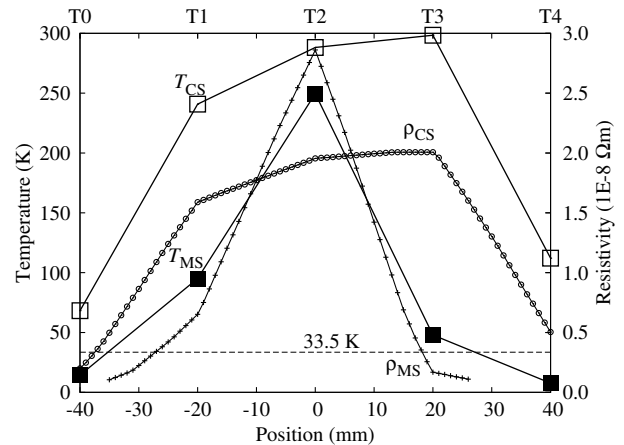


Fig. 7. $T(x)$ for each sample when the power is off ($V_{28} = 0.5$ V). Open squares denote T_{CS} and solid squares for T_{MS} . The data is from Fig. 6b. Open circles are the effective resistivity of the CS sample and crosses are the effective resistivity of the MS sample.

Neglecting the contact resistance between constituent materials in each sample, Eq. (1) can be expressed by

$$\frac{1}{S_{CS}} \int_0^{L_{CS}} \rho_{CS}[T_{CS}(x)] dx = \frac{1}{S_{MS}} \int_0^{L_{MS}} \rho_{MS}[T_{MS}(x)] dx, \quad (2)$$

where S is the cross-sectional area of the sample, L the normal zone length and $\rho(T)$ the sample resistivity, which is a function of the temperature along the length of the normal zone. Because the outer diameters of the wires are the same, we have $S_{CS} = S_{MS}$ and Eq. (2) can be simplified into

$$\overline{\rho_{CS}(T_{CS})} L_{CS} = \overline{\rho_{MS}(T_{MS})} L_{MS}, \quad (3)$$

where $\overline{\rho(T)}$ is the average resistivity of the sample for a certain temperature profile $T(x)$. Since $L_{CS} > L_{MS}$, we have $\overline{\rho_{CS}(T_{CS})} < \overline{\rho_{MS}(T_{MS})}$. This indicates that the shorter normal zone length in the MS sample corresponds to its higher resistivity in addition to lower thermal conductivity. The higher resistivity in the MS sample is mainly due to the Monel outer sheath. The effective resistivity of each sample as a function of temperature is estimated and shown in Fig. 8 with more details given in Appendix A. From Fig. 8, one sees that at the same T above T_c , $\rho_{MS} > \rho_{CS}$, which also explains that $T_{CS}(x) > T_{MS}(x)$ for the same I_t and V_{28} limit.

The average electric field can be estimated by dividing the section voltage by the section length. Fig. 9 shows the electric field across the normal zone and each section for both samples. Since the normal zone in the MS sample does not propagate as far as the CS sample, the electric field along the normal zone is higher in the MS sample than that in the CS sample. For example, $E_{NZ, MS} = 0.524 \text{ V}/0.061 \text{ m} \approx 8.6 \text{ V/m}$ while $E_{NZ, CS} \lesssim 7.0 \text{ V/m}$. Moreover, the end-to-end voltage in the MS sample is primarily from sections V_{24} , V_{25} and V_{26} (see Fig. 2b and Fig. 6a) while it is more distributed in the CS sample because of the longer normal zone. This leads to localized and higher electric field in the MS sample. Only the middle three sections in the MS sample are normal and having electric fields compared to all the five sections in the CS sample. Also $E_{25, MS} \approx 18.2 \text{ V/m}$ while $E_{25, CS} \approx 9.4 \text{ V/m}$, only about 50% $E_{25, MS}$.

Similarly, shorter normal zone length leads to higher spatial temperature gradients in the MS sample compared to the CS sample. The spatial temperature gradient can be calculated by

$$\nabla T_{i,i+1} = \frac{T_i - T_{i+1}}{\Delta x}, \quad (4)$$

where $i = 0, \dots, 3$ and Δx is the interval between adjacent thermocouples (20 mm). From Fig. 6b, one has gradients of -7.7 K/mm between TC1 and TC2 and 10.1 K/mm between TC2 and TC3 in the MS sample. In the CS sample, the gradients are -2.4 K/mm between TC1 and TC2 and -0.5 K/mm between TC2 and TC3, both lower than those in the MS sample.

From Fig. 6a, one sees that the voltage rise is slower in the CS sample, requiring $\sim 3 \text{ s}$ to reach the voltage limit, compared to $\sim 1.5 \text{ s}$ for the MS sample. So the longer normal zone length in

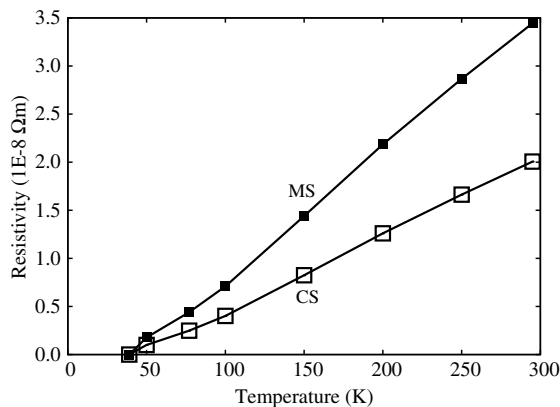


Fig. 8. Effective resistivity for each sample at different temperatures above $T_c = 39 \text{ K}$. More details are given in Appendix A.

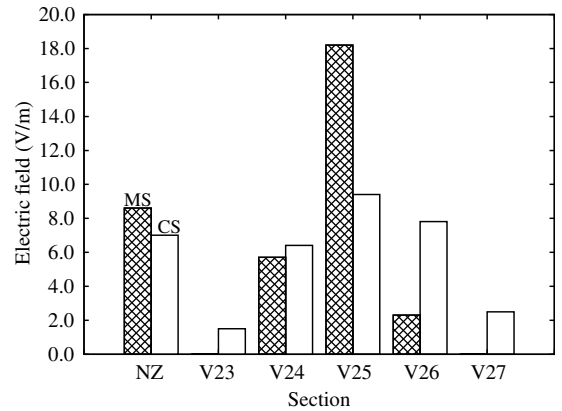


Fig. 9. Electric field comparison for each sample. “NZ” denotes for normal zone. Note that there is no electric field for section V_{23} and V_{27} in the MS sample as there is no voltage across these two sections.

the CS sample may not necessarily imply a faster propagation velocity than in the MS sample. More discussion is given in Section 3.5.

From the quench protection point-of-view, quenches in a magnet wound using conductors with higher resistivity matrix (e.g., the MS sample) may lead to more localized peak voltage and temperature, i.e., higher electric field and temperature gradients, than those in a magnet wound using conductors with lower resistivity matrix (e.g., the CS sample). The time required for quench detection and protection may also be more stringent for a magnet wound using conductors with higher resistivity matrix as the voltage and temperature develop faster.

3.3. Normal zone voltage versus temperature

The normal zone voltage V_{NZ} is one of the possible inputs for quench detection. A higher voltage detection threshold is favorable as the signal/noise ratio will be higher and transient voltage due to ramping will be less problematic. The higher detection threshold, however, may lead to higher hot-spot temperature in a magnet, which may cause permanent failure of the magnet. Thus, the relationship between the V_{NZ} and the hot-spot temperature T_{NZ} may be helpful for the design of the quench detection and protection systems [36,37].

The voltage and temperature of the normal zone are approximately correlated by linearly interpolating the measured $V(t)$ and $T(t)$ quench traces at the same time stamp. Using Fig. 4 as

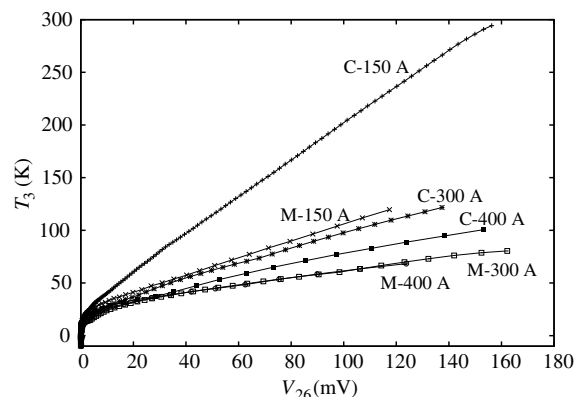


Fig. 10. The normal zone voltage and temperature at section V_{26} for the CS and MS samples measured with different transport currents.

an example, $V_{26} \sim 60$ mV and $T_3 \sim 69$ K at 0.7 s. Fig. 10 shows the T - V correlation for the CS and MS samples with different transport currents. Only section V_{26} is used because (1) less time lag between the $V(t)$ and $T(t)$ compared to the middle (V_{25}) or the end-to-end section (V_{28}); (2) voltage and temperature are higher in this section than those in the end sections.

As shown in Fig. 10, the voltages do not rise until the temperatures reach ~ 25 – 30 K, which correspond to the current sharing temperatures for different transport currents. For voltage higher than 20 mV, T_3 is nearly a linear function of V_{26} for both CS and MS samples. For the same transport current, the CS curve is steeper than the MS curve. Thus when $T_{3,CS} = T_{3,MS}$, $V_{26,MS} > V_{26,CS}$. For example, when $T_3 = 100$ K and $I_t = 150$ A, the voltage on the MS section is 93 mV while it is only 42 mV in the CS section. This indicates that for the same temperature limit and transport current, the normal zone voltage may be higher in a magnet wound using conductors with higher resistivity matrix (e.g., the MS sample) than in a magnet wound using conductors with lower resistivity matrix (e.g., the CS sample). Thus quench detection based on the normal zone voltage may be easier in a magnet wound using the MS type conductors. For the same normal zone voltage and transport current, the temperature of the CS sample is higher than that of the MS sample, which is consistent with Fig. 6.

With higher transport current, the slope of the T - V curves of both samples decreases. Using the CS sample as an example, the slope reduces from ~ 1.8 K/mV at 150 A to ~ 0.7 K/mV at 300 A. For the same temperature, the normal zone voltage increases with constant temperature when the $T(V)$ curve becomes flatter. This indicates that quench detection and protection may be easier for a magnet running at high transport current than at low transport current [38]. Note however that the MS $T(V)$ curves measured at 300 A and 400 A overlap which implies that the $T(V)$ curves may converge at higher transport currents. For the MS sample, the curves start converging at $I_t = 400$ A ($\sim 40\%I_c$). So one could still limit the transport current in a magnet for enough stability margin and at the same time take advantage of the flatter $T(V)$ curve.

3.4. Quench energy

The minimum quench energy (MQE) used to quench the sample is measured as a function of transport current. In this case, MQE refers to the resistive energy generated by pulsing the heater as described in Section 2. The actual heat into the sample is seen in Eq. (5), where the heat absorbed in the epoxy and the helium are subtracted from the heater energy. Since the sample and heater geometries are identical, one can directly compare the behavior of the MS and CS samples. Note that the heat generated by the samples themselves due to current sharing is also not accounted for here [38]

$$E_{\text{sample}} = E_{\text{htr}} - E_{\text{epo}} - E_{\text{helium}}, \quad (5)$$

Here, we neglect E_{helium} . The quench energies of both samples are comparable because E_{helium} will not vary. The energy absorbed by the epoxy is found to be generally less than 10% of that generated by the heater and is also neglected (see Appendix B). So the quench energy reported here is simply E_{htr} . Note that these values are higher than the intrinsic MQE that would quench real magnets, especially when the magnet quench is initiated by heat in a location with no direct contact to cryogen.

Fig. 11 shows the MQE versus normalized transport current (I_t/I_c) for the MS and CS samples. Two samples of each type are measured and the results are reproducible. The MQE decreases with increasing transport current. The MQE of the CS sample decreases 80% from 2.36 J to 0.46 J when I_t increases from $0.13I_c$ to $0.28I_c$; the MQE of the MS sample decreases 48% from 0.79 J to 0.49 J for a similar I_t increase. For $I_t > 0.39I_c$, the CS sample has a

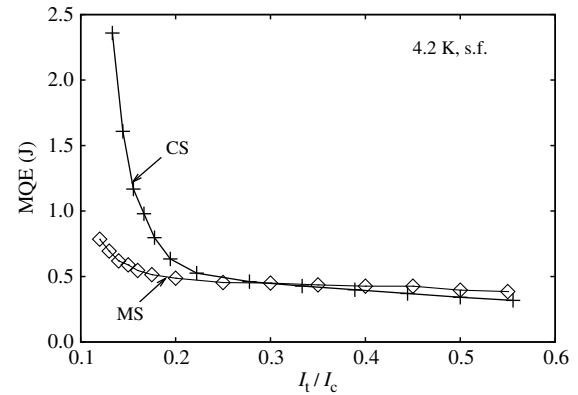


Fig. 11. MQE of the MS and the CS samples as a function of the normalized transport current. + is for the CS sample and \diamond is for the MS sample.

MQE decreasing at ~ 0.55 mJ/A while the MS sample has a slower rate of ~ 0.26 mJ/A. At higher current, the MS sample has a MQE slightly higher than that of the CS sample, which may be due to the larger number and smaller diameter of the filaments in the MS sample.

Quench behavior of similar samples were measured in an adiabatic environment [24]. When I_t/I_c increases from 0.5 to 0.8, the MQE of a similar MS sample decreases from 8 mJ to 5 mJ at 5 K, 4.80 T and the MQE of a CS sample decreases from 30 mJ to 15 mJ at 5 K, 3.51 T [24]. Note that these values are 20% of the total heat input generated by the heater used in the experiments [24]. Because of the cooling provided by the liquid helium in this study, the actual energy that initiates the quench will be lower than E_{htr} . A one order-of-magnitude difference between the MQEs of NbTi and Nb₃Sn measured in an adiabatic condition as compared to liquid helium is shown in [39]. The 300 ms pulse duration may also contribute to the higher MQE reported here [40].

In contrast to the MQE difference between the samples measured adiabatically [24], the MQE of the MS sample is marginally higher than that of the CS sample for $I_t/I_c \gtrsim 0.3$ in this study. This indicates that the Glidcop outer sheath may have limited impact on the stability, which is consistent with what Tsukamoto et al. found in a numerical comparison of the MQEs of a multifilamentary NbTi tapes with a Cu matrix and a Cupronickel matrix [41]. Musenich et al., however, found that a coil wound with lower matrix resistance has a higher quench current [11].

Compared to the typical MQE of low- T_c superconductors, e.g., 10–100 μ J for NbTi conductor [40], the MQE of the MgB₂ samples is much higher and hence more stable. It is expected that MgB₂ coils may be less sensitive to the energy release associated with epoxy cracking or conductor movement that are thought to be one of the common quench triggers for low- T_c magnets.

3.5. Normal zone propagation velocity

The normal zone propagation velocity (NZPV) is estimated by dividing the distance between the voltage taps by the time delay between the voltage traces for a fixed reference voltage (V_{ref}) [42,43,38]. This is the average speed of the normal zone propagation in the section between the two voltage taps. Linear interpolation is used to estimate the data point for the specific V_{ref} . The voltage traces for the NZPV measurements are all initiated by the MQE at each transport current level as shown in Fig. 11. Traces of V_{26} and V_{27} are used to estimate the NZPV. The resolution for the CS sample is 10 ms/pt and 400 μ s/pt for the MS sample. The NZPV error due to the resolution can be expressed by $r/(t+r)$, where r is the resolution and t is the time for the normal zone to

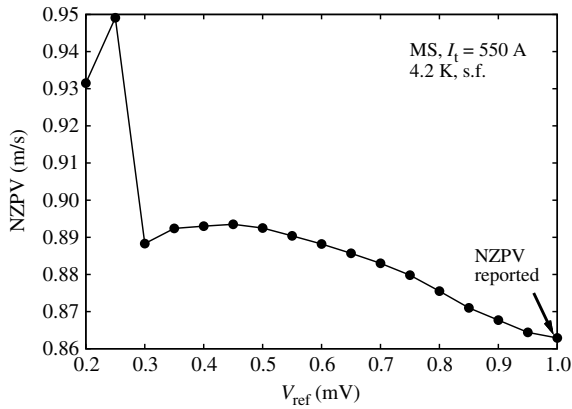


Fig. 12. Normal zone propagation velocity as a function of reference voltage. Data measured on the MS sample with $I_t = 550$ A.

travel the section. The estimated NZPV will be a lower bound because the actual time interval is not greater than the estimated one. So for a velocity of 1 m/s and a section of 20 mm long, the NZPV based on a resolution of 10 ms/pt could be at most 33% lower than the actual value. An error of 9.1% corresponds to a velocity of 0.2 m/s with a resolution of 10 ms/pt.

The beginning of the voltage rise of a section indicates a normal zone enters that section. Thus the V_{ref} should be as low as possible. However, because of the noise level and the limited time resolution of the measurement, a fixed $V_{ref} = 1$ mV is chosen to report the NZPV values for both samples. To show the V_{ref} dependence of the NZPV, Fig. 12 gives an example of the NZPV of the MS sample as a function of V_{ref} with a step-size of 0.05 mV. When V_{ref} varies from 0.2 mV to 1.0 mV, NZPV decreases from 0.95 m/s to 0.87 m/s, a 8.4% variation.

To illustrate the V_{ref} dependence of NZPV, error bars are used to denote the lower and upper bounds of the NZPV given by the corresponding $V_{ref, min}$ (~ 0.1 – 0.2 mV) and $V_{ref, max}$ (1 mV), as shown in Fig. 13.

I_t increases from $\sim 15\%I_c$ to $\sim 90\%I_c$, the NZPVs of both samples increase from 15 mm/s to ~ 1 m/s. This trend is also found in Refs. [6,7,21–23,25]. The results are close to those reported at 4.2 K with similar current ratios [21,23]. A similar MS sample, measured at 5 K and 4.80 T, has a NZPV ranging from 160 mm/s to 390 mm/s when I_t/I_c ranges from 0.5 to 0.8. A similar CS sample

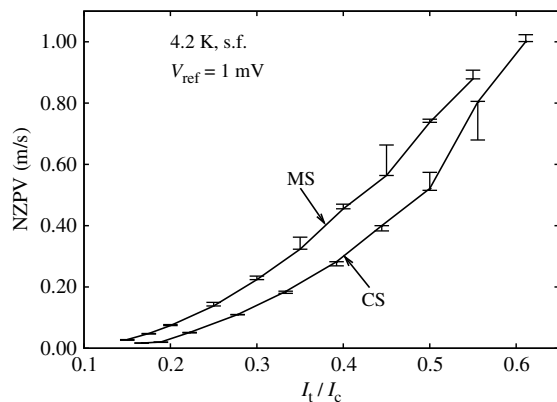


Fig. 13. Normal zone propagation velocity of the MS and the CS samples as a function of normalized transport current. $V_{ref} = 1$ mV. Error bars represent the V_{ref} dependence of NZPV.

measured at 5 K and 3.51 T gives 75 mm/s to 175 mm/s [24]. These values are less than 20% of those in this study at similar normalized current. The difference may result from the significantly lower I_c in a background field and slightly higher measurement temperature. For example, $I_c = 45$ A at 5 K and 4.80 T for a MS sample in [24] while in this study, $I_c = 1000$ A in self-field and at 4.2 K. Thus, the Joule heating that drives the growth of normal zone is much lower in-field than that of the self-field case even though the wire is close to its critical surface in the adiabatic case ($I_t/I_c = 0.8$) [24].

Since the I_c of MgB_2 is strongly field-dependent, it indicates that for an application like MRI where the wire sees a field of 1–3 T, the NZPV may be lower than that in for example, a transformer, where the field may be as low as 0.15–0.20 T [6]. The NZPV may increase however with higher applied field as the in-field critical current increases. For example, if the in-field transport current is higher than 550 A ($55\%I_c$) based on Fig. 13, the high NZPV (~ 1 m/s) may still be achievable for some applications.

From Fig. 13, one also sees that the NZPV of the MS sample is higher than that of the CS sample, consistent with the discussion in Section 3.2. This is also consistent with the results given by the adiabatic experiments [24]. The difference, however, tends to become smaller with the increasing current, given the increasing uncertainty due to the low sampling frequency on the CS sample at higher current level.

4. Conclusion

Self-field quench behavior of two types of multifilamentary MgB_2 round wires are measured in liquid helium. One type of sample has six filaments and a Glidcop outer sheath. The other has 18 filaments and a Monel outer sheath. Both samples have a Cu matrix. The normal zone is initiated by a heater wound around the sample.

For the same transport current and end-to-end voltage, the normal zone is shorter in the Monel-sheathed sample with higher matrix resistivity than the Glidcop-sheathed sample, which leads to higher electric fields and spatial temperature gradients in the Monel-sheathed sample during the quench. The time required for quench detection and protection may also be more stringent for a magnet wound by conductors with a higher resistivity matrix as the voltage and temperature develop faster. For the same normal zone temperature and transport current, however, the voltage across the normal zone is higher in the Monel-sheathed sample than that in the Glidcop-sheathed sample, which may make the quench detection based on normal zone voltage easier in a magnet wound by conductors with higher matrix resistivity.

The quench energies of both samples decrease with increasing transport current. For transport current greater than 300 A ($\sim 30\%I_c$), the quench energy of the Monel-sheathed sample is marginally higher than that of the Glidcop-sheathed sample. The role of the lower matrix resistivity in the Glidcop-sheathed sample for stability and protection may not be significant. The normal zone propagation velocities of both samples are similar and increase from 15 mm/s at 150 A to ~ 1 m/s at 550 A ($\sim 55\%I_c$).

Acknowledgements

The authors thank M. Rindfleisch, K. McFadden and M. Tomsic of Hyper Tech Research Inc. for providing the samples; X. T. Liu, T. Effio and H. Song, all with National High Magnetic Field Laboratory (NHMFL), for help in the experiments and discussions. This work was supported in part by the U.S. Department of Energy through the Center for Advanced Power Systems at Florida State University and the National Science Foundation through the NHMFL.

Appendix A. Resistivity and resistance of the wire sample above T_c

In this section, we estimate the effective resistivity of each sample above the T_c , 39 K. For temperature below the T_c , the sample effective resistivity depends on the T_{cs} and hence the I_t . When $T \geq T_{cs}$, the effective resistivity is determined by the normal metal in the conductor; when $T < T_{cs}$, the effective resistivity is zero. The contact resistance between adjacent constituent material layers is neglected and each material is assumed to be electrically in parallel. Uniform temperature on the sample cross-section is also assumed. The effective resistivity of the CS sample is given by

$$\rho_{CS} = \frac{\rho_{PC} \rho_{GC} \rho_{SC} S}{\rho_{PC} \rho_{GC} S_{SC} + \rho_{PC} \rho_{SC} S_{GC} + \rho_{GC} \rho_{SC} S_{PC}}, \quad (A.1)$$

where “PC” stands for the pure Cu matrix, “SC” for superconductor, “GC” for Glidcop, “S” the sample cross-sectional area. Typical Glidcop has a resistivity higher than but close to that of Cu. For example, Glidcop C15715, with 0.3% wt Al_2O_3 , has a resistivity of 8.8% higher than that of Cu (C10200) from room temperature to 77 K [44]. Thus with $\rho_{GC} \geq \rho_{Cu}$, Eq. (A.1) could be simplified to

$$\rho_{CS} = \frac{\rho_{Cu} \rho_{SC} S}{\rho_{Cu} S_{SC} + \rho_{SC} S_{Cu}} = \frac{\rho_{Cu} \rho_{SC}}{\rho_{Cu} \lambda_{CS} + \rho_{SC} (1 - \lambda_{CS})}, \quad (A.2)$$

where $S_{Cu} = S_{PC} + S_{GC}$, $\lambda_{CS} = 0.16$ the fill factor. Similarly, the effective resistivity of the MS sample is given by

$$\rho_{MS} = \frac{\rho_{Cu} \rho_{Mo} \rho_{SC} S}{\rho_{Cu} \rho_{Mo} S_{SC} + \rho_{Cu} \rho_{SC} S_{Mo} + \rho_{Mo} \rho_{SC} S_{Cu}} = \frac{\rho_{Cu} \rho_{Mo} \rho_{SC}}{\rho_{Cu} \rho_{Mo} \lambda_{MS} + \rho_{Cu} \rho_{SC} \beta + \rho_{Mo} \rho_{SC} (1 - \lambda_{MS} - \beta)}, \quad (A.3)$$

where “Mo” denotes Monel and $\lambda_{MS} = 0.17$. The ratio between the area of the Monel sheath and that of the sample’s cross section is defined as β and $\beta = 1 - (1 - 2\xi)^2$, where ξ is the ratio between the thickness of the outer sheath and the diameter of the sample. ξ is found to be 0.1 by measuring directly in Fig. 1b using GIMP [45].

The resistivity data for Cu (RRR = 100) and Monel from 10 K to 295 K can be found in [46]. The resistivity of MgB_2 is from [28]. For simplicity, we assume $T_{cs} = T_c$ ($I_t \rightarrow 0$) and the effective resistivity is set 0 below 39 K. The effective resistivity of each sample is estimated using Eqs. (A.2) and (A.3) as a function of temperature and shown in Fig. 8. Note that because the Glidcop outer sheath is replaced by pure Cu in Eq. (A.2), the actual effective resistivity of the CS sample will be higher.

One can estimate the normal zone resistance in the sample by

$$R = \frac{1}{S} \int_0^L \rho[T(x)] dx \approx \frac{\Delta x}{S} \sum_{i=0}^N \rho[T(x_i)], \quad (A.4)$$

where L the length of the normal zone. The normal zone length is found by crossing the temperature criterion and the temperature profile as shown in Fig. 7. The temperature criterion is set to 33.5 K, the current sharing temperature for a transport current of 150 A. Let $\Delta x = 1$ mm, the resistance between TC0 and TC4 in the CS sample is 2.195 m Ω and the normal zone resistance in the MS sample is 1.154 m Ω . The estimated values are on the same order as those indicated by the measurements ($R_{CS} = 3.707$ m Ω and $R_{MS} = 3.493$ m Ω). The error may result from the material properties and the accuracy of the temperature profile.

Appendix B. Estimation of the quench energy

The energy input by the heater is calculated by

$$E_{\text{htr}} = \int_0^{t_p} V(t) I(t) dt, \quad (B.1)$$

where t_p is the heater pulse duration (300 ms), $V(t)$ the voltage across and $I(t)$ the current flow into the heater. Both $V(t)$ and $I(t)$ are measured by the DPO with a data rate of 2.5 kHz. In practice, Eq. (B.1) is calculated by numerical integration of the measured $V(t)$ and $I(t)$ traces. The uncertainty of the pulse width measurement (± 10 ms) translates into $\sim 7\% E_{\text{htr}}$. Since the heater voltage is varied with the highest resolution of 0.01 V, the resolution in MQE is less than 10 mJ.

The energy absorbed by the epoxy is calculated by

$$E_{\text{epo}} = m \int_{T_0}^{T_1} C_{\text{epo}}(T) dT, \quad (B.2)$$

where m is the epoxy mass, T_0 is the initial temperature, and T_1 is the peak temperature of the epoxy due to the heat pulse. Since thermocouple TC2 is fixed atop of the epoxy, its reading may be used as T_1 [38]. The reading of TC2 is usually higher than the actual T_1 due to the heat generation from the sample when in current sharing. Thus, T_1 is used for the case with a heat pulse just below the MQE that corresponds to the maximum recovery energy. Another assumption is that the temperature inside the epoxy is relatively uniform and there is no temperature gradient between the epoxy and the sample [38].

The mass of epoxy used to glue the heater to the MS samples is 2.2 mg while it is about 6.5 mg for the CS samples. Using the same method discussed in Ref. [38], we found the energy absorbed by the epoxy is less than 10% of the energy generated by the heater.

Similarly, the peak temperatures due to the maximum recovery energy for both samples are found to be similar and thus we assume similar heat transfer to the helium for both samples.

References

- [1] Scanlan RM, Malozemoff AP, Larbalestier DC. Superconducting materials for large scale applications. Proc IEEE 2004;92(10):1639–54.
- [2] Cooley LD, Ghosh AK, Scanlan RM. Costs of high-field superconducting strands for particle accelerator magnets. Supercond Sci Technol 2005;18:R51–65.
- [3] Iwasa Y, Larbalestier DC, Okada M, Penco R, Sumption MD, Xi X. A round table discussion on MgB_2 toward a wide market or a niche production? – a summary. IEEE Trans Appl Supercond 2006;16(2):1457–64.
- [4] Collings EW, Kawabata S, Bhatia M, Tomsic M, Sumption MD. Magnesium diboride superconducting strand for accelerator and light source applications. IEEE Trans Appl Supercond 2006;16(2):1445–8.
- [5] Vinod K, Abhilash Kumar RG, Syamaprasad U. Prospects for MgB_2 superconductors for magnet application. Supercond Sci Technol 2007;20:R1–R13.
- [6] Tomsic M, Rindfleisch M, Yue J, McFadden K, Phillips J, Sumption MD, et al. Overview of MgB_2 superconductor applications. Int J Appl Ceram Technol 2007;4:250–9.
- [7] Tomsic M, Rindfleisch M, Yue J, McFadden K, Doll D, Phillips J, et al. Development of magnesium diboride (MgB_2) wires and magnets using in situ strand fabrication method. Physica C 2007;456:203–8.
- [8] Arda L, Sacli OA, Tomsic M, Dur O, Hascicek YS. Field dependence of the critical current density of MgB_2/Cu wire for coil development. Supercond Sci Technol 2007;20:1054–8.
- [9] Sumption MD, Bhatia M, Rindfleisch M, Tomsic M, Collings EW. Transport properties of multifilamentary, *in situ* route, Cu-stabilized MgB_2 strands: one metre segments and the $J_c(B, T)$ dependence of short samples. Supercond Sci Technol 2006;19:155–60.
- [10] Giunchi G, Ripamonti G, Perini E, Cavallin T, Bassani E. Advances in the reactive liquid Mg infiltration technique to produce long superconducting MgB_2 tubular wires. IEEE Trans Appl Supercond 2007;17(2):2761–5.
- [11] Musenich R, Fabbriatore P, Farinon S, Ferdeghini C, Grasso G, Greco M, et al. Behavior of MgB_2 react & wind coils above 10 K. IEEE Trans Appl Supercond 2005;15(2):1452–6.
- [12] Tanaka K, Kitaguchi H, Kumakura H, Yamada H, Hirakawa M, Okada M. Fabrication and transport properties of an MgB_2 solenoid coil. Supercond Sci Technol 2005;18:678–81.
- [13] Sumption MD, Bhatia M, Buta F, Bohnenstiehl S, Tomsic M, Rindfleisch M, et al. Solenoidal coils made from monofilamentary and multifilamentary MgB_2 strands. Supercond Sci Technol 2005;18:961–5.
- [14] Bascuñán J, Lee H, Bobrov ES, Hahn S, Iwasa Y, Tomsic M, et al. IEEE Trans Appl Supercond 2006;16(2):1427–30.
- [15] Bellomo G, Musenich R, Sorbi M, Volpini G. MgB_2 coils for particle accelerators. IEEE Trans Appl Supercond 2006;16(2):1439–41.
- [16] Magnusson N, Rundle M. A 200 kW MgB_2 induction heater project. J Phys: Conf Ser 2006;43:1019–22.

- [17] Sumption MD, Bhatia M, Buta F, Bohnenstiehl S, Tomsic M, Rindfleisch M, et al. Multifilamentary MgB₂-based solenoidal and racetrack coils. *Physica C* 2007;458:12–20.
- [18] Musenich R, Greco M, Razeti M, Tavilla G. Electrical characterization of a multi-strand MgB₂ cable. *Supercond Sci Technol* 2007;20:235–8.
- [19] Alessandrini M, Musenich R, Penco R, Grasso G, Nardelli D, Marabotto R, et al. Behavior of a 14 cm bore solenoid with multifilament MgB₂ tape. *IEEE Trans Appl Superconduct* 2007;17(2):2252–7.
- [20] Ye L, Majoros M, Campbell AM, Coombs T, Harrison S, Sargent P, et al. Investigations of current limiting properties of the MgB₂ wires subjected to pulse overcurrents in the benchtop tester. *Supercond Sci Technol* 2007;20(4):320–6.
- [21] Fu M, Xu X, Jiao Z, Kumakura H, Togano K, Ding L, et al. Minimum quench energy and normal zone propagation velocity in MgB₂ superconducting tape. *Physica C* 2004;402(3):234–8.
- [22] Fu M, Pan Z, Jiao Z, Kumakura H, Togano K, Ding L, et al. Quench characteristics and normal zone propagation of an MgB₂ superconducting coil. *Supercond Sci Technol* 2004;17:160–3.
- [23] van Weeren H, van den Eijnden N, Wessel W, Lezza P, Schlachter S, Goldacker W, et al. Adiabatic normal zone development in MgB₂ superconductors. *IEEE Trans Appl Superconduct* 2005;15(2):1667–70.
- [24] van Weeren H. Magnesium diboride superconductors for magnet applications. Ph.D. thesis. University of Twente; 2007. <<http://purl.org/utwente/58096>>.
- [25] Martínez E, Lera F, Martínez-López M, Yang Y, Schlachter S, Lezza P, et al. Quench development and propagation in metal/MgB₂ conductors. *Supercond Sci Technol* 2006;19:143–50.
- [26] Gambardella U, Saggese A, Sessa P, Guarino A, Pace S, Masullo G, et al. Stability measurements in multifilamentary MgB₂ tapes. *IEEE Trans Appl Superconduct* 2007;17(2):2937–40.
- [27] Ye L, Majoros M, Campbell AM, Coombs T, Astill D, Harrison S, et al. Experimental studies of the quench behavior of MgB₂ superconducting wires for fault current limiter applications. *Supercond Sci Technol* 2007;20:621–8.
- [28] Stenvall A, Korpela A, Mikkonen R, Grasso G. Stability considerations of multifilamentary MgB₂ tape. *Supercond Sci Technol* 2006;19:184–9.
- [29] Stenvall A, Korpela A, Mikkonen R, Grasso G. Quench analysis of MgB₂ coils with a ferromagnetic matrix. *Supercond Sci Technol* 2006;19:581–8.
- [30] Majoros M, Campbell AM, Glowacki BA, Tomov RI. Numerical modeling of heating and current-sharing effects on *I*–*V* curves of Y₁Ba₂Cu₃O₇ and MgB₂ conductors. *Physica C* 2004;401:140–5.
- [31] Glowacki BA, Majoros M, Tanaka K, Kitaguchi H, Kumakura H, Okada M, et al. Critical current and cryogenic stability modelling of filamentary MgB₂ conductors. *J Phys: Conf Ser* 2006;43:103–6.
- [32] Ekin JW. Experimental techniques for low-temperature measurements. Oxford University Press; 2006. p. 290–3, [chapter 7.3.4].
- [33] Holúbek T, Kováč P, Melisek T. Current transfer length in MgB₂/Fe mono-core wire and approximation of the interface layer resistivity. *Supercond Sci Technol* 2005;18:1218–21.
- [34] Holúbek T, Dhallé M, Kováč P. Current transfer in MgB₂ wires with different sheath materials. *Supercond Sci Technol* 2007;20:123–8.
- [35] Dresner L. Stability of superconductors. New York: Plenum Press; 1995. p. 36–7, [chapter 3].
- [36] Iwasa Y, Sinclair MW. Protection of large superconducting magnets: maximum permissible undetected quench voltage. *Cryogenics* 1980;20(12):711–4.
- [37] Dresner L. On the connection between normal zone voltage and hot spot temperature in uncooled magnets. *Cryogenics* 1994;34(2):111–8.
- [38] Wang X, Trociewitz UP, Schwartz J. Near-adiabatic quench experiments on short YBa₂Cu₃O_{7-δ} coated conductors. *J Appl Phys* 2007;101(5):053904.
- [39] Baynham DE, Edwards VW, Wilson MN. Transient stability of high current density superconducting wires. *IEEE Trans Magnet* 1981;17(1):732–5.
- [40] Bauer P. Stability of superconducting strands for accelerator magnets. Ph.D. thesis. Vienna University of Technology; 1998.
- [41] Tsukamoto O, Nakada M. Stability of high-current-density composite superconductor subject to pulsive and local disturbance. *IEEE Trans Magnet* 1985;21(2):370–3.
- [42] Trillaud F, Palanki H, Trociewitz UP, Thompson SH, Weijers HW, Schwartz J. Normal zone propagation experiments on HTS composite conductors. *Cryogenics* 2003;43:271–9.
- [43] Wang X, Caruso AR, Breschi M, Zhang G, Trociewitz UP, Weijers HW, et al. Normal zone initiation and propagation in Y–Ba–Cu–O coated conductors with Cu stabilizer. *IEEE Trans Appl Superconduct* 2005;15(2):2586–9.
- [44] Troxell JD. Glidcop dispersion strengthened copper: potential application in fusion power generators. In: Proceedings of IEEE thirteenth symposium on fusion engineering; 1989. p. 761–5.
- [45] GNU image manipulation program. <<http://www.gimp.org/>>.
- [46] Ekin JW. Experimental techniques for low-temperature measurements. Oxford University Press; 2006. p. 575–6, [chapter A6, Properties of solids at low temperature].